

# On the split Voigt profile and its use in the analysis of X-ray diffraction patterns

F. Sánchez-Bajo

*Departamento de Física Aplicada, Escuela de Ingenierías Industriales, Universidad de Extremadura, Avda de Elvas s/n. 06006 Badajoz (Spain).*

Received 16 July 2024; accepted 19 November 2024

The main properties (integral breadth, FWHM, Fourier transform) of the split Voigt function have been analysed. These are important in the study of the X-ray diffraction peaks. In this way, some X-ray diffraction lines of a sample of quartz and zirconia have been analysed by using single line methods, describing the instrumental-spectral asymmetric peaks by means of split Voigt functions.

*Keywords:* X-ray diffraction; split Voigt function; line-broadening.

DOI: <https://doi.org/10.31349/RevMexFis.71.021004>

## 1. Introduction

The Voigt function has been extensively employed in several fields related to the Physics, from the Astrophysics [1] to the Materials Science and Crystallography [2–4], to describe symmetric bell-shape distributions. This function is the convolution of a Gaussian and a Cauchy functions and it can be expressed as

$$V(x) = \frac{I_o \beta_C}{\exp(k^2) \operatorname{erfc}(k)} \int_{-\infty}^{+\infty} \frac{\exp(-\pi \frac{y^2}{\beta_G^2})}{\beta_C^2 + \pi^2(x-y)^2} dy, \quad (1)$$

being  $x = u - u_o$ ,  $I_o$ , the maximum of the peak,  $\beta_C$  and  $\beta_G$ , the corresponding Cauchy and Gauss integral breadths, respectively, and  $k = \beta_C / \sqrt{\pi} \beta_G$ . In the definition of  $x$ ,  $u$  represents the independent variable, being  $u_o$  the position of the maximum. In the case of a stellar spectral line, for example,  $u$  is a wavelength, whereas in a neutron or X-ray diffraction patterns, is an angular unit (usually degrees). A summary of the main properties of the Voigt function can be found elsewhere [5]. Note that, in many situations, simplest approximations of the Voigt function, as the pseudo-Voigt [6] or the Pearson VII [7] functions can be used.

These functions have been widely used in the analysis of individual or group X-ray diffraction peaks as well as in programs that analyse the whole diffractogram, as FullProf [8], GSAS-II [9] or TOPAS<sup>i</sup>, within the framework of the Rietveld method [10]. Thus, function shape and breadth parameters can be used to evaluate microstructural information (domain size and micro-strains, etc) in polycrystalline samples. Similar programs, as MAUD [11] or MarqX [12] -based on the Whole Powder Pattern Fitting (WPPF) technique-, also can provide microstructural data, but using physical models instead of empirical (although based usually in a physical background, as is the case of the Voigt function) peak shapes. Note that, although the use of these programs have been proposed especially from the Crystallography, in many cases, within the more specific Material Science topics, traditional techniques based on the use of a limited set of peaks continue being employed with success.

Although the aforementioned functions are symmetric (for example, Voigt function is a convolution of two symmetric functions), however, in certain cases, the X-ray diffraction bell-shape distributions are not symmetric. This behaviour appears, for example, in the X-ray diffraction peaks (especially at low angles), due to the presence of instrumental features as the axial divergence of the X-ray incident beam [13] or microstructural details, as planar defects [14]. These effects limit the use of symmetric approximations to bell-shape functions, as the Voigt or its aforementioned approximations. By this reason, different approaches has been employed to describe asymmetric lines, as the substitution of the symmetric function by the product of an asymmetric and a symmetric functions. In the case of the Voigt function, asymmetries have been taken into account by means of power series expansion [15], but a simplest analytic way is the use of split functions, where the left and right halves of the profile are modelled by using different shape parameters. This approach has been extensively used with the approximations of the Voigt functions, and, in the particular case of the Voigt function, program Fityk [16] include the split Voigt function among the shape functions for the analysis of X-ray diffraction peaks, although no explicit details about the analytic expression are contained in the manual<sup>ii</sup>.

Asymmetric nature of the split Voigt function makes it an adequate alternative to model X-ray diffraction peaks in the cases where these show departures from symmetric shapes. This modelling can be performed within programs that analyse the whole diffraction pattern or individual or group peaks.

Due to the lack of information about the mathematical properties of the split Voigt function (relevant in the analysis of the X-ray diffraction peaks -or other bell-shape distributions-), in this work I have analysed the most interesting ones. In regard to this, the next section is devoted to the mathematical characteristics of the split Voigt function (with special emphasis in the width measures and their approximations). Subsequently, a simple application to the X-ray diffraction analysis will be showed, and then the main conclusions shall be presented. Owing to the extension of the

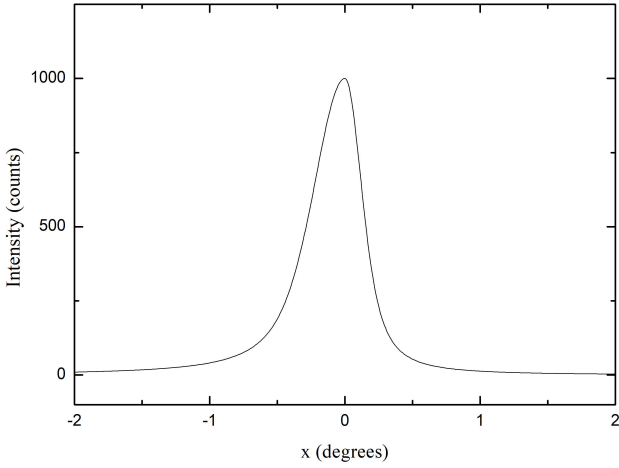


FIGURE 1. Graphic of a split Voigt simulated X-ray diffraction peak. Note that the simulation has been performed to generate a peak clearly asymmetric to the left, as it is sometimes usual in low-angle X-ray powder diffraction data.

mathematical background, a significant part of that has been included in a final supplementary section.

## 2. Mathematical core

### 2.1. Definition

The split Voigt function can be defined as

$$sV(x) = \begin{cases} \frac{I_o \beta_{Cl}}{\exp(k_l^2) \operatorname{erfc}(k_l)} \int_{-\infty}^{+\infty} \frac{\exp\left(-\pi \frac{y^2}{\beta_{Gl}^2}\right)}{\beta_{Cl}^2 + \pi^2 (x-y)^2} dy & x \leq 0, \\ \frac{I_o \beta_{Cr}}{\exp(k_r^2) \operatorname{erfc}(k_r)} \int_{-\infty}^{+\infty} \frac{\exp\left(-\pi \frac{y^2}{\beta_{Gr}^2}\right)}{\beta_{Cr}^2 + \pi^2 (x-y)^2} dy & x \geq 0, \end{cases} \quad (2)$$

where the subindices  $l$  and  $r$  correspond, respectively, to the left and right halves of the profile. As example, Fig. 1 displays the graphic of a split Voigt function simulating a X-ray diffraction profile with  $I_o = 1000$  counts,  $\beta_{Cl} = 0.5^\circ$ ,  $\beta_{Cr} = 0.3^\circ$ ,  $\beta_{Gl} = 0.4^\circ$  and  $\beta_{Gr} = 0.2^\circ$ .

### 2.2. Continuity

Note that the split Voigt function must fulfill the requirement of continuity in all the points. This condition implies, in particular, that the function must be continuous at  $x = 0$ . The definition of the preceding subsection implies that the split Voigt function is continuous in  $\Re$  (details in Supplementary material section A).

### 2.3. Integral breadth

Integral breadth is defined as the quotient of the area under the distribution and the maximum of the peak, that is

$$\beta = \frac{\int_{-\infty}^{+\infty} sV(x) dx}{I_o}. \quad (3)$$

Substituting Eqs. (2) in (3) one can obtain (Supplementary material section B)

$$\beta = \frac{\beta_l + \beta_r}{2}, \quad (4)$$

where  $\beta_l$  and  $\beta_r$  are the corresponding left-handed and right-handed integral breadths.

Note that, according to Eq. (3)

$$\int_{-\infty}^{+\infty} sV(x) dx = \beta I_o. \quad (5)$$

By dividing Eq. (2) by the product  $\beta I_o$ , we have the normalized split Voigt function of area unit.

#### 2.3.1. Approximations to the integral breadth

Equation (4) can be approximated in several forms, from the starting point of the integral breadth of the Voigt function. One possibility is the use of the Halder and Wagner [17] equation

$$\beta^2 \approx \beta_C \beta + \beta_G^2, \quad (6)$$

that leads to

$$\beta = \frac{\beta_C + \sqrt{\beta_C^2 + 4\beta_G^2}}{2} = \frac{\beta_G}{2} (\sqrt{\pi} k + \sqrt{4 + \pi k^2}), \quad (7)$$

or

$$\frac{\beta}{\beta_G} = \frac{1}{2} \left( \sqrt{\pi} k + \sqrt{4 + \pi k^2} \right). \quad (8)$$

According to this result, the integral breadth of the split Voigt function could be expressed as

$$\beta \approx \frac{\beta_{Gl} (\sqrt{\pi} k_l + \sqrt{4 + \pi k_l^2}) + \beta_{Gr} (\sqrt{\pi} k_r + \sqrt{4 + \pi k_r^2})}{4}. \quad (9)$$

Other approximation uses the Padé approximant of order  $[M/N]$ , defined as a rational function in the form [18]

$$R(x) = \frac{\sum_{i=0}^{M} a_i x^i}{1 + \sum_{j=1}^{N} b_j x^j}. \quad (10)$$

In this case, the Padé approximant of order  $[3/4]$  of  $\beta/\beta_G$  for a Voigt function is

$$\frac{\beta}{\beta_G} \approx \frac{\sum_{i=0}^{3} a_i k^i}{1 + \sum_{j=1}^{4} b_j k^j}, \quad (11)$$

with  $a_1 = 1.435323$ ,  $a_2 = 0.732884$ ,  $a_3 = 0.134554$ ,  $b_1 = 0.306943$ ,  $b_2 = 0.113296$ ,  $b_3 = -0.00934741$  and  $b_4 = 0.00133085$ .

In this way, the corresponding integral breadth of the split Voigt function is

$$\beta \approx \frac{1}{2} \left( \beta_{Gl} \frac{\sum_{i=0}^{3} a_i k_l^i}{1 + \sum_{j=1}^{4} b_j k_l^j} + \beta_{Gr} \frac{\sum_{i=0}^{3} a_i k_r^i}{1 + \sum_{j=1}^{4} b_j k_r^j} \right). \quad (12)$$

Finally, the integral breadth of the Voigt function can be approximated by using the rational expression [19]

$$1 - \operatorname{erf}(x) = (c_1 t + c_2 t^2 + c_3 t^3 + c_4 t^4 + c_5 t^5) \exp(-x^2), \quad (13)$$

with  $t = (1/1 + px)$ , where  $p = 0.3275911$ ,  $c_1 = 0.254829592$ ,  $c_2 = -0.284496736$ ,  $c_3 = 1.421413741$ ,  $c_4 = -1.453152027$  and  $c_5 = 1.061405429$ .

Now, the Eq. (13) leads to

$$\frac{\beta}{\beta_G} \approx \frac{1}{c_1 t + c_2 t^2 + c_3 t^3 + c_4 t^4 + c_5 t^5}. \quad (14)$$

According to the Eq. (14), the approximation of the corresponding split Voigt function can be expressed as

$$\beta \approx \frac{1}{2} \left( \frac{\beta_{Gl}}{\sum_{i=1}^{i=5} c_i t^i} + \frac{\beta_{Gr}}{\sum_{i=1}^{i=5} c_i t^i} \right). \quad (15)$$

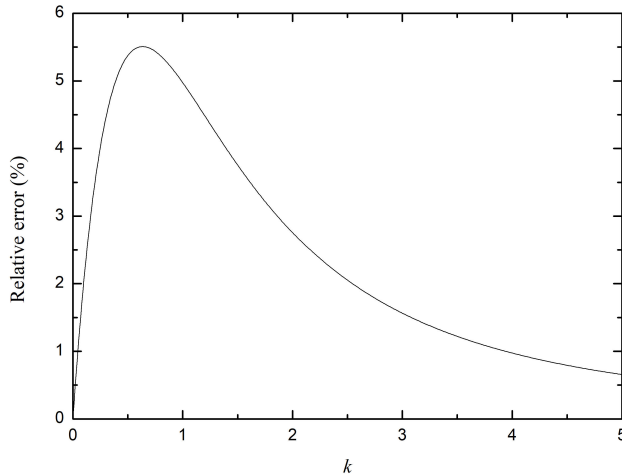


FIGURE 2. Relative error of  $\beta/\beta_G$  (in %) as function of  $k$  for the approximation done by the Eq. (8).

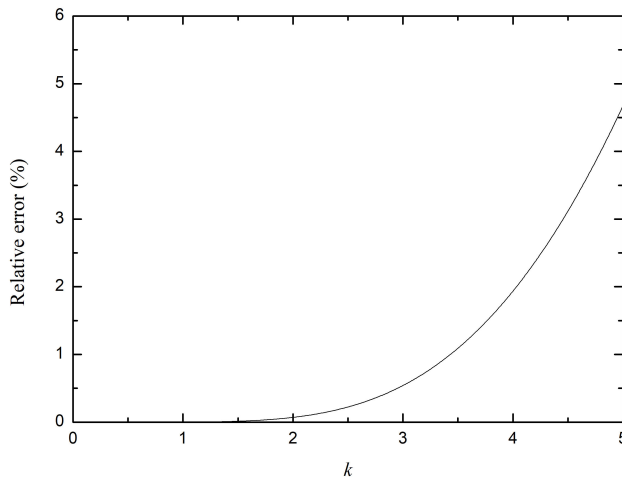


FIGURE 3. Relative error of  $\beta/\beta_G$  (in %) as function of  $k$  for the approximation done by the Eq. (11).

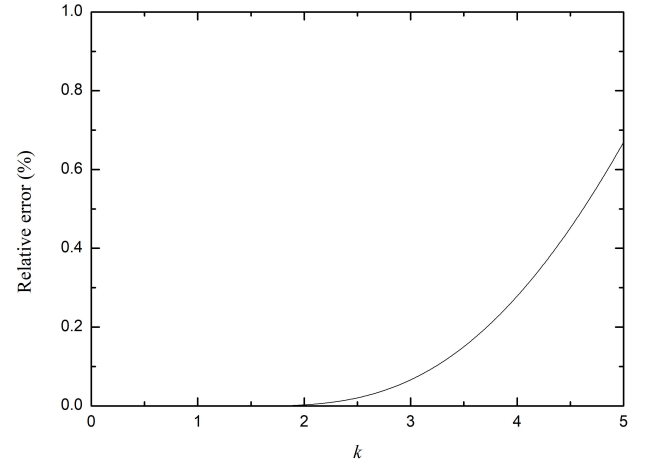


FIGURE 4. Relative error of  $\beta/\beta_G$  (in %) as function of  $k$  for the approximation done by the Eq. (14).

Figures 2, 3 and 4 display the relative error in the determination of  $\beta/\beta_G$  by using the Eqs. (8), (11) and (14) as function of  $k$ . Note that, for the sake of simplicity (due to the similarity between the left and right-handed parts of the approximations to the integral breadth of the split Voigt function), these figures are referred to the Voigt function.

In this way, the Y-scale in Fig. 4 is different from Figs. 2 and 3, indicating that the rational approximation done by Eq. (13) is the best. In regard to this, the X-scale is limited to  $k = 5.0$  because this value is very close to the Lorentzian or Cauchy limit of the Voigt function. This assures that the above figures are representative of the most cases.

#### 2.4. Full width at half maximum

Other well-known measure of the width of a bell-shape type function is the Full Width at Half Maximum (FWHM), or range of the independent variable  $x$  where the function value is greater or equal that the maximum value divided by two. In the case of the Voigt function (and, obviously, of the split Voigt function), no simple equation exists to describe the FWHM (designed as  $2w$ ), that is defined as the solution of the equation [5]

$$\Re \left( \omega \left[ \frac{\sqrt{\pi} w}{\beta_G} + ik \right] \right) = \frac{\beta_G}{2\beta} = \operatorname{erfc}(k) \exp(k^2), \quad (16)$$

where  $\Re(\omega[z])$  is the real part of the complex error function and  $w$  is the Half Width at Half Maximum (HWHM), or (FWHM/2), for symmetric profiles.

Equation (16) can be approximated by [20]

$$2w \approx \frac{2\beta_G}{\sqrt{\pi}} \sqrt{1 + k^2}. \quad (17)$$

From (17) it is easy to obtain the corresponding approximation for a split Voigt function, taking into account that, now, that the FWHM,  $2w$ , can be expressed as  $2w = w_l + w_r$ ,  $w_l$  and  $w_r$  being, respectively, the corresponding left-handed

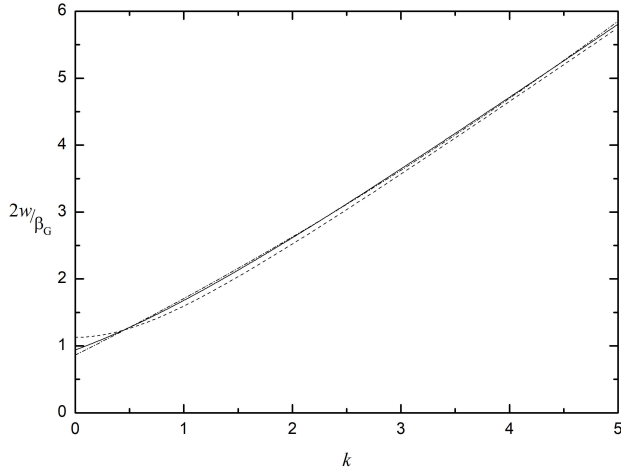


FIGURE 5.  $2w/\beta_G$  values as function of  $k$ : Voigt function (solid line), Posener approximation (dashed line) and parabolic approximation (dashed-dotted line).

and right-handed HWHM of the profile. Thus, the Posener split Voigt approximation for the FWHM can be written as

$$2w = w_l + w_r \approx \frac{\beta_{Gl}}{\sqrt{\pi}} \sqrt{1 + k_l^2} + \frac{\beta_{Gr}}{\sqrt{\pi}} \sqrt{1 + k_r^2}. \quad (18)$$

A simple (and better) parabolic approximation of the FWHM for a Voigt function can be derived as

$$\frac{2w}{\beta_G} \approx 0.86479 + 0.80459k + 0.03853k^2. \quad (19)$$

Using Eq. (19) in the case of the split Voigt function, the following equation is obtained

$$2w \approx \frac{\beta_{Gl}}{2} (0.86479 + 0.80459k_l + 0.03853k_l^2) + \frac{\beta_{Gr}}{2} (0.86479 + 0.80459k_r + 0.03853k_r^2). \quad (20)$$

Figures 5 and 6 show the values of  $2w/\beta_G$  and the relative error, respectively, for the Posener and parabolic approximations (for the Voigt function, for the sake of simplicity).

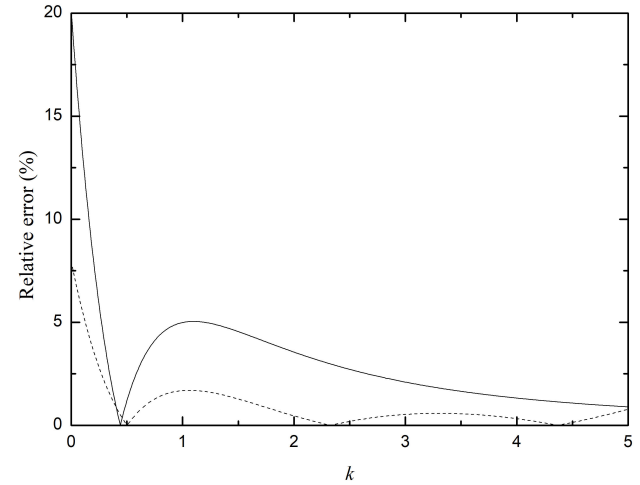


FIGURE 6. Relative error of  $2w/\beta_G$  (in %) as function of  $k$  for the Posener (solid line) and parabolic (dashed line) approximations.

## 2.5. Moments

In X-ray diffractometry, moments as the centroid or the variance are of the maximum interest in the analysis of the peaks (for example, in the well-known variance method). However, in the case of the split Voigt function, the centroid is not well defined (Supplementary material section C) and the classic definition of the variance in X-ray diffractometry is compromised. Nevertheless, the variance method of the X-ray line broadening analysis can still be applied by using the split Voigt function [21] because the variance coefficients are obtained from the variance-range function and are independent of the centroid value.

## 2.6. Fourier transform

The Fourier transform of the split Voigt function can be defined as

$$F(t) = \int_{-\infty}^{+\infty} sV(x) \exp(2\pi ixt) dx. \quad (21)$$

After some mathematical manipulation (Supplementary material section D), Eq. (21) leads to

$$F(t) = \frac{I_o \beta_{Cl}}{\exp(k_l^2) \operatorname{erfc}(k_l)} \frac{\beta_{Gl}}{2} \exp(-\pi \beta_{Gl}^2 t^2) \left( \beta_{Cl}^{-1} \exp(-2\beta_{Cl} t) - \int_{-\infty}^{+\infty} \frac{\exp(2\pi iyt)}{\beta_{Cl}^2 + \pi^2 y^2} \operatorname{erf} \left[ \frac{\sqrt{\pi}}{\beta_{Gl}} y + \sqrt{\pi} \beta_{Gl} t i \right] dy \right) + \frac{I_o \beta_{Cr}}{\exp(k_r^2) \operatorname{erfc}(k_r)} \frac{\beta_{Gr}}{2} \exp(-\pi \beta_{Gr}^2 t^2) \left( \beta_{Cr}^{-1} \exp(-2\beta_{Cr} t) + \int_{-\infty}^{+\infty} \frac{\exp(2\pi iyt)}{\beta_{Cr}^2 + \pi^2 y^2} \operatorname{erf} \left[ \frac{\sqrt{\pi}}{\beta_{Gr}} y + \sqrt{\pi} \beta_{Gr} t i \right] dy \right). \quad (22)$$

The above equation is different from 1 at  $t = 0$ . In regard to this, putting  $t = 0$  and taking into account the odd character of the error function, Eq. (22) leads to

$$F(0) = \frac{I_o}{2} \left[ \frac{\beta_{Gl}}{\exp(k_l^2) \operatorname{erfc}(k_l)} + \frac{\beta_{Gr}}{\exp(k_r^2) \operatorname{erfc}(k_r)} \right]. \quad (23)$$

Thus, the normalized Fourier transform ( $= 1$  at  $t = 0$ ) is  $F(t)/F(0)$ . It can be easily demonstrated that, for  $\beta_{Cl} = \beta_{Cr}$  and  $\beta_{Gl} = \beta_{Gr}$  the Fourier transform of the split Voigt function reduces to the corresponding expression of the Voigt function.

### 3. Application example

#### 3.1. Mathematical core

In this section, I apply simple line broadening approaches that can be used with asymmetric profiles, as the described by split Voigt functions. Note that, although more sophisticated procedures has been developed recently, as the Whole Powder Pattern Modelling or WPPM [22], classic simplified single or multiple line methods -as the Williamson-Hall [23] or Warren-Averbach [24] procedures- are widely used to study the microstructure of materials by X-ray diffractometry. In the case of single line techniques, the main advantage associated to the simplicity of the collection and analysis of the experimental data, contrasts with the need of additional hypotheses about the dependence of the shape parameters or related quantities on the microstructural features.

In this way, a simple procedure to evaluate mean values of some microstructural parameters was developed by [25], using as starting point the basic equations of the kinematical diffraction theory. That equations are

$$\left(\frac{dF^S(t)}{dt}\right)_{t \rightarrow 0} = \left(\frac{dF(t)}{dt}\right)_{t \rightarrow 0} = -\frac{1}{\langle t \rangle_a}, \quad (24)$$

and

$$\ln F(t) = \ln F^S(t) - 2\pi^2 d_{hkl}^{-2} t^2 \langle e^2 \rangle, \quad (25)$$

where  $F(t)$  is now the Fourier transform and  $F^S(t)$  is the size-component of the Fourier transform, both referred to the “pure” profile<sup>iii</sup>. In the above equations,  $\langle t \rangle_a$  is the area-weighted average column length perpendicular to the reflecting  $hkl$  planes,  $d_{hkl}$ , the interplanar spacing, and  $\langle e^2 \rangle$ , the square of the root-mean-squared (r.m.s.) microstrain. The equation (25) is strictly valid for a gaussian strain distribution or for  $t \rightarrow 0$ . In these cases,  $\langle e^2 \rangle$  can be expressed as

$$\langle e^2 \rangle = -\frac{1}{4\pi^2 d_{hkl}^{-2}} [F''(t)_{t \rightarrow 0} - F^{S''}(t)_{t \rightarrow 0}]. \quad (26)$$

A simple inspection of Eqs. (24) and (26) shows that  $\langle t \rangle_a$  can be obtained from the analysis of a “pure” single line Fourier transform. By contrast, the determination of the r.m.s microstrain requires: a) the analysis of multiple lines (strictly speaking, belonging to the same family of crystallographic planes) or b) additional hypotheses about  $F^S(t)$  or

its second derivative at  $t = 0$ . In regard to the point b) it has been an usual practice in X-ray diffractometry to assume that crystallite or domain size effects are associated to a Cauchy component whereas r.m.s. strain is related to a Gaussian dependence. Thus, this leads to a expression of  $F(t)$  in the form

$$F(t) = \exp(-at - bt^2), \quad (27)$$

where  $a = 1/\langle t \rangle_a$  and  $b = 2\pi^2 d_{hkl}^{-2} \langle e^2 \rangle$ , being  $F^S(t) = \exp(-at)$ . Note that Eq. (27) is clearly consistent with Eqs. (24) and (25).

On the other hand, the term associated with the second derivative of  $F^S(t)$  can be dropped assuming that the area-weighted column length distribution fulfills the condition  $p_s(0) = 0$  [26]. Thus, Eqs. (24) and (26) can be used to obtain  $\langle t \rangle_a$  and  $\langle e^2 \rangle$  from the first and second derivatives of the “pure” profile Fourier transform at  $t = 0^{iv}$ . Also, it is possible, by considering the exponential dependence of  $F^S(t)$ , to obtain the equation

$$F^{S''}(t)_{t \rightarrow 0} = \langle t \rangle_a^{-2}. \quad (28)$$

In this way, we must be cautious with the above hypotheses. Note, for example, that the r.m.s. strain must be positive. This implies that, if we assume  $F^{S''}(t)_{t \rightarrow 0} = 0$ , the second derivative  $F''(t)_{t \rightarrow 0}$  must be negative. Or, if we assume the exponential dependence for  $F^S(t)$ ,  $F''(t)_{t \rightarrow 0} - F^{S''}(t)_{t \rightarrow 0}$  must also be negative, in order to provide a r.m.s. strain positive. These constraints has been analyzed, in the case of the Voigt function, by [25]. This is the price to pay in the single line approaches with analytical models.

Note that above equations assume that the only microstructural effects are those associated with the crystallite size and micro-strains. In this case, the Fourier transform  $F(t)$  in Eqs. (24) and (25) is the cosine Fourier transform, defined as [27]

$$F_c(t) = \frac{H_c(t)G_c(t) + H_s(t)G_s(t)}{G_c^2(t) + G_s^2(t)}, \quad (29)$$

where  $H_c(t)$  and  $H_s(t)$  are the cosine and sine Fourier transform of the experimental profile, respectively, whereas  $G_c(t)$  and  $G_s(t)$  are the corresponding cosine and sine Fourier transform of the instrumental-spectral profile. From (29), the first derivative can be expressed as

$$\begin{aligned} F_c'(t) &= \frac{H_c'(t)G_c(t) + H_c(t)G_c'(t)}{G_c^2(t) + G_s^2(t)} \\ &+ \frac{H_s'(t)G_s(t) + H_s(t)G_s'(t)}{G_c^2(t) + G_s^2(t)} \\ &- 2 \frac{F_c(t)(G_c'(t)G_c(t) + G_s(t)G_s'(t))}{G_c^2(t) + G_s^2(t)}, \end{aligned} \quad (30)$$

whereas the second derivative is

$$\begin{aligned}
F_c''(t) = & [8(G_c(t)H_c(t) + G_s(t)H_s(t))(G_c(t)G_c'(t) + G_s(t)G_s'(t))^2 - 4(G_c^2(t) + G_s^2(t))(G_c(t)G_c'(t) \\
& + G_s(t)G_s'(t))(H_c(t)G_c'(t) + H_s(t)G_s'(t) + G_c(t)H_c'(t) + G_s(t)H_s'(t)) - 2(G_c^2(t) + G_s^2(t))(G_c(t)H_c(t) \\
& + G_s(t)H_s(t))(G_c'^2(t) + G_s'^2(t) + G_c(t)G_c''(t) + G_s(t)G_s''(t)) + (G_c^2(t) + G_s^2(t))^2(2G_c'(t)H_c'(t) \\
& + 2G_s'(t)H_s'(t) + H_c(t)G_c''(t) + H_s(t)G_s''(t) + G_c(t)H_c''(t) + G_s(t)H_s''(t))] (G_c^2(t) + G_s^2(t))^{-3}. \quad (31)
\end{aligned}$$

Although Eqs. (30) and (31) are simplified in the limit  $t \rightarrow 0$ , in this particular analysis we can draw on the symmetrical character of the “pure” profile. Thus, the sine Fourier transform of this profile is zero and Eq. (29) reduces to

$$F_c(t) = \frac{H_c(t)}{G_c(t)}. \quad (32)$$

In this way, the corresponding first and second derivatives are now

$$F_c'(t) = \frac{H_c'(t)G_c(t) - H_c(t)G_c'(t)}{G_c^2(t)} = \frac{H_c'(t)}{G_c(t)} - \frac{H_c(t)G_c'(t)}{G_c^2(t)}, \quad (33)$$

and

$$F_c''(t) = -\frac{H_c(t)G_c''(t)}{G_c^2(t)} - \frac{2G_c'(t)H_c'(t)}{G_c^2(t)} + \frac{2H_c(t)G_c'^2(t)}{G_c^3(t)} + \frac{H_c''(t)}{G_c(t)}, \quad (34)$$

respectively.

Note that these last equations, in the limit  $t \rightarrow 0$  and combined with Eqs. (24) and (26), provide  $\langle t \rangle_a$  and  $\langle e^2 \rangle$ . In regard to this, analytical shape functions are needed in order to obtain the derivatives included in Eqs. (33) and (34). Moreover, assuming the normalization of the  $H_c(t)$  and  $G_c(t)$  functions at  $t = 0$  (that is,  $H_c(0) = G_c(0) = 1$ ), Eqs. (33) and (34) lead to [25]

$$F_c'(0) = H_c'(0) - G_c'(0), \quad (35)$$

and

$$F_c''(0) = -G_c''(0) - 2G_c'(0)H_c'(0) + 2G_c'^2(0) + H_c''(0). \quad (36)$$

Now, assuming split Voigt functions to describe the experimental and instrumental-spectral profiles, the corresponding normalized cosine Fourier transforms are

$$\begin{aligned}
H_c(t) = & \frac{\frac{\beta_{G_{lh}} \exp(-2\beta_{C_{lh}}t - \pi\beta_{G_{lh}}^2 t^2)}{\exp(k_{lh}^2) \operatorname{erfc}(k_{lh})} + \frac{\beta_{G_{rh}} \exp(-2\beta_{C_{rh}}t - \pi\beta_{G_{rh}}^2 t^2)}{\exp(k_{rh}^2) \operatorname{erfc}(k_{rh})}}{\frac{\beta_{G_{lh}}}{\exp(k_{lh}^2) \operatorname{erfc}(k_{lh})} + \frac{\beta_{G_{rh}}}{\exp(k_{rh}^2) \operatorname{erfc}(k_{rh})}}, \quad (37)
\end{aligned}$$

and

$$\begin{aligned}
G_c(t) = & \frac{\frac{\beta_{G_{lg}} \exp(-2\beta_{C_{lg}}t - \pi\beta_{G_{lg}}^2 t^2)}{\exp(k_{lg}^2) \operatorname{erfc}(k_{lg})} + \frac{\beta_{G_{rg}} \exp(-2\beta_{C_{rg}}t - \pi\beta_{G_{rg}}^2 t^2)}{\exp(k_{rg}^2) \operatorname{erfc}(k_{rg})}}{\frac{\beta_{G_{lg}}}{\exp(k_{lg}^2) \operatorname{erfc}(k_{lg})} + \frac{\beta_{G_{rg}}}{\exp(k_{rg}^2) \operatorname{erfc}(k_{rg})}}, \quad (38)
\end{aligned}$$

where the subindices  $h$  and  $g$  indicate the character of the profile (experimental and instrumental-spectral, respectively). Note that, as I have previously pointed out, the odd character of the error function implies that the corresponding sine Fourier transforms at  $t = 0$  are null ( $H_s(0) = G_s(0) = 0$ ).

Thus, from Eqs. (37) and (38), the first derivatives at  $t = 0$  of the normalized cosine Fourier transforms are obtained as

$$\begin{aligned}
H_c'(0) = & -2 \left[ \frac{\frac{\beta_{C_{lh}}\beta_{G_{lh}}}{\exp(k_{lh}^2) \operatorname{erfc}(k_{lh})} + \frac{\beta_{C_{rh}}\beta_{G_{rh}}}{\exp(k_{rh}^2) \operatorname{erfc}(k_{rh})}}{\frac{\beta_{G_{lh}}}{\exp(k_{lh}^2) \operatorname{erfc}(k_{lh})} + \frac{\beta_{G_{rh}}}{\exp(k_{rh}^2) \operatorname{erfc}(k_{rh})}} \right], \quad (39)
\end{aligned}$$

and

$$G'_c(0) = -2 \left[ \frac{\frac{\beta_{Clg}\beta_{Glg}}{\exp(k_{lg}^2) \operatorname{erfc}(k_{lg})} + \frac{\beta_{Crg}\beta_{Gr g}}{\exp(k_{rg}^2) \operatorname{erfc}(k_{rg})}}{\frac{\beta_{Glg}}{\exp(k_{lg}^2) \operatorname{erfc}(k_{lg})} + \frac{\beta_{Gr g}}{\exp(k_{rg}^2) \operatorname{erfc}(k_{rg})}} \right], \quad (40)$$

and the corresponding second derivatives at  $t = 0$  can be expressed as

$$H''_c(0) = \frac{\frac{(4\beta_{Clh}^2 - 2\pi\beta_{Glh}^2)\beta_{Glh}}{\exp(k_{lh}^2) \operatorname{erfc}(k_{lh})} + \frac{(4\beta_{Crh}^2 - 2\pi\beta_{Grh}^2)\beta_{Grh}}{\exp(k_{rh}^2) \operatorname{erfc}(k_{rh})}}{\frac{\beta_{Glh}}{\exp(k_{lh}^2) \operatorname{erfc}(k_{lh})} + \frac{\beta_{Grh}}{\exp(k_{rh}^2) \operatorname{erfc}(k_{rh})}}, \quad (41)$$

and

$$G''_c(0) = \frac{\frac{(4\beta_{Clg}^2 - 2\pi\beta_{Glg}^2)\beta_{Glg}}{\exp(k_{lg}^2) \operatorname{erfc}(k_{lg})} + \frac{(4\beta_{Crg}^2 - 2\pi\beta_{Gr g}^2)\beta_{Gr g}}{\exp(k_{rg}^2) \operatorname{erfc}(k_{rg})}}{\frac{\beta_{Glg}}{\exp(k_{lg}^2) \operatorname{erfc}(k_{lg})} + \frac{\beta_{Gr g}}{\exp(k_{rg}^2) \operatorname{erfc}(k_{rg})}}. \quad (42)$$

Substituting Eqs. (39), (40), (41), (42) in Eqs. (35) and (36) allows to evaluate  $\langle t \rangle_a$  and  $\langle e^2 \rangle$  for the crystallographic direction corresponding to the profile. Note that, if the integral breadth is expressed in degrees ( $2\theta$ ), as it is usual, it must be transformed to reciprocal units (longitude<sup>-1</sup>) by using the conversion factor

$$C = \frac{\pi \cos \theta_o}{180\lambda}, \quad (43)$$

where  $\lambda$  is the radiation wavelength and  $\theta_o$  is the position of the maximum intensity of the peak.

### 3.2. Experiments and results

I have applied the procedure depicted in the preceding section to a sample of zirconia ( $\text{ZrO}_2$ ) and  $\beta$ - $\text{SiO}_2$  (quartz), where two polytypes of zirconia, tetragonal (t) and monoclinic (m), are present. X-ray diffraction experiments were performed in a Philips PW-1800 diffractometer, using  $\text{CuK}\alpha$  radiation ( $\lambda = 0.154183$  nm) and graphite monochromator in the incident beam. The generator settings were 40 kV and 35 mA. The step-scanning technique was used with a step of 0.05 degrees ( $2\theta$ ) and a counting time of 5 s/step. X-ray diffraction data were collected over a range of 25-90 degrees ( $2\theta$ ). Figure 7 displays the 25-33 degrees section of the diffraction pattern, where the stronger peaks are present. The peaks correspond to the 101 quartz ( $2\theta_o \approx 26.7^\circ$ ), 11-1 m- $\text{ZrO}_2$  ( $2\theta_o \approx 28.3^\circ$ ), 101 t- $\text{ZrO}_2$  ( $2\theta_o \approx 30.3^\circ$ ) and 111 m- $\text{ZrO}_2$  ( $2\theta_o \approx 31.4^\circ$ ) lines. In this way, I have used these peaks in the single-line analyses presented here.

A sample of  $\alpha$ - $\text{Al}_2\text{O}_3$  (corundum) was used as instrumental-spectral standard. Reflections of this sample were scanned in the same conditions as the experimental sample, but with a step of 0.01 degrees ( $2\theta$ ), due to the smaller widths of the peaks, and a counting time of 10 s/step. In particular, 012 ( $2\theta_o \approx 25.6^\circ$ ), 104 ( $2\theta_o \approx 35.2^\circ$ ), 110 ( $2\theta_o \approx 37.8^\circ$ ), 113 ( $2\theta_o \approx 43.4^\circ$ ), 024 ( $2\theta_o \approx 52.6^\circ$ ), 116 ( $2\theta_o \approx 57.5^\circ$ ), 214 ( $2\theta_o \approx 66.5^\circ$ ) and 300 ( $2\theta_o \approx 68.2^\circ$ ) lines were selected to perform the X-ray diffraction experi-

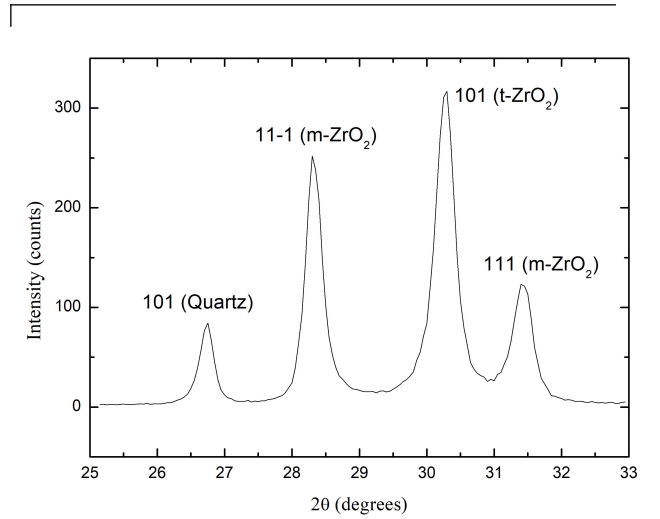


FIGURE 7. X-ray diffraction pattern of the experimental sample. Labeled are the  $hkl$  Miller indices of the peaks, besides the corresponding phase. Note that the data are corrected by the Lorentz-polarization factor. The reflections include the two components of the  $\text{CuK}\alpha$  doublet.

ments. As example, Fig. 8 shows the X-ray diffraction pattern corresponding to the 104 and 110 corundum peaks.

Figure 8 shows clearly the asymmetric character of the instrumental-spectral peaks, that it is specially noticeable in the low-angle zone of the diffraction pattern. By contrast, the

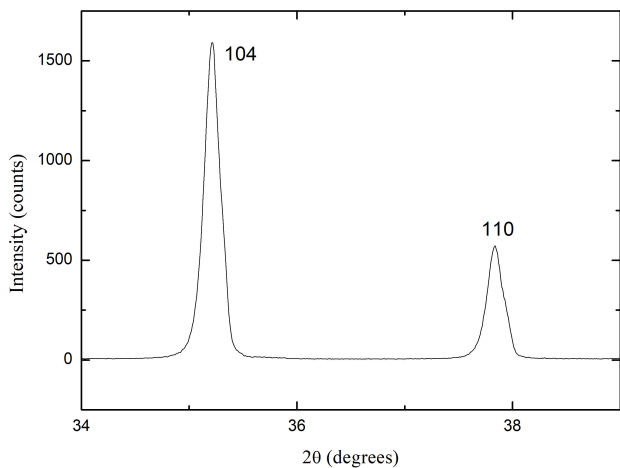


FIGURE 8. X-ray diffraction pattern of the 104 and 110 instrumental-spectral sample. As in the experimental X-ray diffraction pattern, the data have been corrected by the Lorentz-polarization factor.

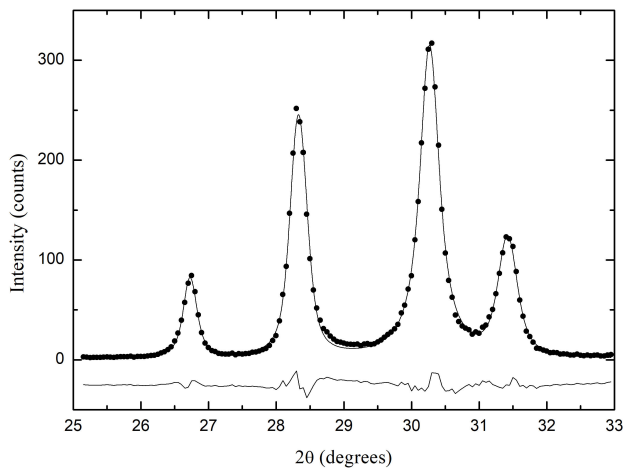


FIGURE 9. Result of the fit of Voigt functions to the X-ray diffraction peaks of the experimental sample. Data points are represented by dark circles and the fit by the solid line. The line at the bottom is the difference plot (observed minus calculated).

experimental profile shows peaks almost symmetric (the small asymmetries are due to the peak overlap). By these reasons, on the modelling of the peaks, I have used Voigt functions for the experimental peaks and split Voigt functions for the instrumental-spectral peaks. Thus, Fig. 9 displays the model fit to the experimental peaks and Fig. 10, the model fit corresponding to the instrumental-spectral corundum 012 peak. In this way, Table I present the results of the fits of Voigt functions to the different peaks of the experimental sample. Similarly, Table II shows the corresponding results of the fits of split Voigt functions to the instrumental-spectral peaks.

As the positions of the experimental peaks does not correspond exactly with those of the instrumental-spectral peaks, I have analysed the dependence with the angle of the width

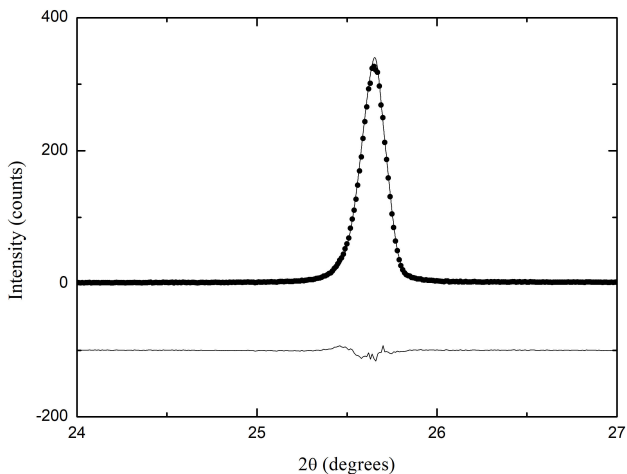


FIGURE 10. Result of the fit of a split Voigt function to the 012 instrumental-spectral peak. Data points are represented by dark circles and the fit by the solid line. The line at the bottom is the difference plot (observed minus calculated).

TABLE I. Parameters of the fit to the experimental peaks. Numbers between parentheses are the standard deviation referred to the last significant digit. The Goodness-of-Fit (GofF), defined as  $\text{GofF} = (\chi_r^2)^{1/2} = \sqrt{\chi^2/(N-P)}$ , where  $N$  is the number of data and  $P$  the number of fitted parameters, was 3.08. A linear empirical function was used to describe the background, as it is usual in the case of well crystallized samples, and, for the sake of simplicity, the background parameters are not included in this table.

Peak	$\beta_C(^{\circ})$	$\beta_G(^{\circ})$	$2\theta_o(^{\circ})$	$I_o(\text{counts})$
101 quartz	0.25(2)	0.121(3)	26.7071(11)	56(2)
11-1 m-ZrO <sub>2</sub>	0.251(7)	0.197(9)	28.3084(8)	168(2)
101 t-ZrO <sub>2</sub>	0.483(3)	0.079(7)	30.2428(7)	218(2)
111 m-ZrO <sub>2</sub>	0.35(1)	0.186(6)	31.3962(13)	82(2)

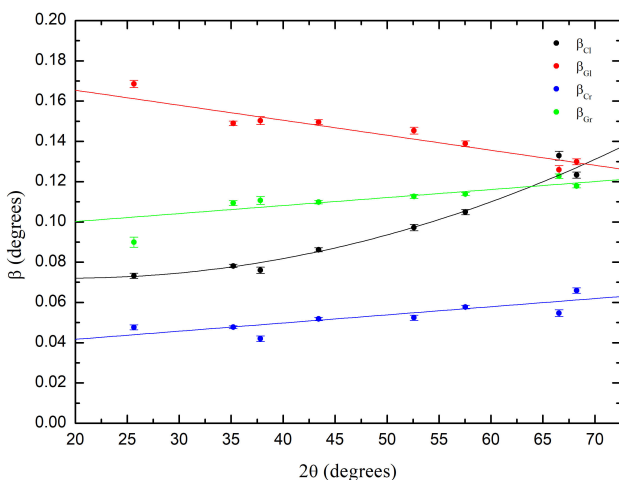


FIGURE 11. Result of the quadratic ( $\beta_{Cl}$ ) and linear ( $\beta_{Gl}$ ,  $\beta_{Gr}$  and  $\beta_{Gr}$ ) fits to the integral breadth parameters of the instrumental-spectral corundum peaks. Data points are represented by dark circles and the fit by the solid line (in the same colour for each integral breadth).

TABLE II. Parameters of the fit to the instrumental-spectral peaks. Numbers between parentheses are the standard deviation referred to the last significant digit. As in the case of the experimental peaks, a linear function was used to describe the background, whose parameters are not included in this table.

Peak	$\beta_{Cl}(\circ)$	$\beta_{Gl}(\circ)$	$\beta_{Cr}(\circ)$	$\beta_{Gr}(\circ)$	$2\theta_o(\circ)$	$I_o(\text{counts})$	Goff
012	0.073(1)	0.169(2)	0.048(1)	0.090(3)	25.6472(10)	248(2)	2.08
104	0.0781(8)	0.149(1)	0.0477(7)	0.109(1)	35.2006(5)	1286(4)	2.98
110	0.076(2)	0.150(2)	0.042(1)	0.111(2)	37.8266(8)	473(3)	2.98
113	0.087(1)	0.146(1)	0.0518(8)	0.1099(9)	43.4009(4)	1655(5)	2.98
024	0.097(2)	0.145(2)	0.052(1)	0.113(1)	52.5942(5)	1216(5)	2.36
116	0.103(1)	0.144(1)	0.0570(9)	0.1135(7)	57.5367(3)	2771(7)	2.98
214	0.133(2)	0.126(2)	0.055(2)	0.123(1)	66.5499(4)	1529(6)	2.20
300	0.123(2)	0.130(2)	0.066(1)	0.1178(9)	68.2382(3)	2479(8)	2.20

TABLE III. Instrumental-spectral shape parameters at the position of the experimental peaks (angle). Numbers between parentheses are the standard deviation referred to the last significant digit

Angle ( $\circ$ )	$\beta_{Cl}(\circ)$	$\beta_{Gl}(\circ)$	$\beta_{Cr}(\circ)$	$\beta_{Gr}(\circ)$
26.7071	0.073(3)	0.160(3)	0.044(2)	0.103(3)
28.3084	0.074(2)	0.159(3)	0.045(2)	0.104(3)
30.2428	0.075(2)	0.158(3)	0.046(2)	0.104(3)
31.3962	0.075(2)	0.157(2)	0.046(2)	0.105(2)

parameters of the later. Figure 11 displays the integral breadths of the instrumental-spectral peaks as functions of  $2\theta_o$ , along with linear and quadratic fits to these data.

Table III shows the values of the instrumental-spectral shape parameters at the position of the experimental peaks, according to the fits included in Fig. 11.

By using equations involving the first and second derivatives of the “pure” cosine Fourier transforms in terms of the shape parameters, I have calculated  $\langle t \rangle_a$  and  $\langle e^2 \rangle$  from Eqs. (24) and (26). Note that, in this case, the results lead to positive  $F_c''(0)$  values. By this reason, the condition  $F_c'''(t)_{t \rightarrow 0} = 0$  can not be assumed. In regard to this, I also have used the Eq. (28). Moreover, I have evaluated microstructural parameters by approximating the “pure” cosine Fourier transform using the model defined by Eq. (27). As example, Fig. 12 shows this approximation for the case of the 101 quartz peak. Table IV displays the obtained microstructural parameters.

Results of Table IV shows the limitations of the approximations of the function  $F_c''(t)$  in the case of a single line approach, particularly in the evaluation of the r.m.s. microstrain. Note that this drawback is not related with the use of symmetric or asymmetric profiles in the description of the peaks, because it can be also appear in classic analyses with symmetric lines. Note that, according Eq. (26), the condition  $F_c'''(t)_{t \rightarrow 0} > F_c''(t)_{t \rightarrow 0}$  must be fulfilled. Moreover, as the second derivative of the Fourier size transform is proportional to the column length distribution [27], also must be positive.

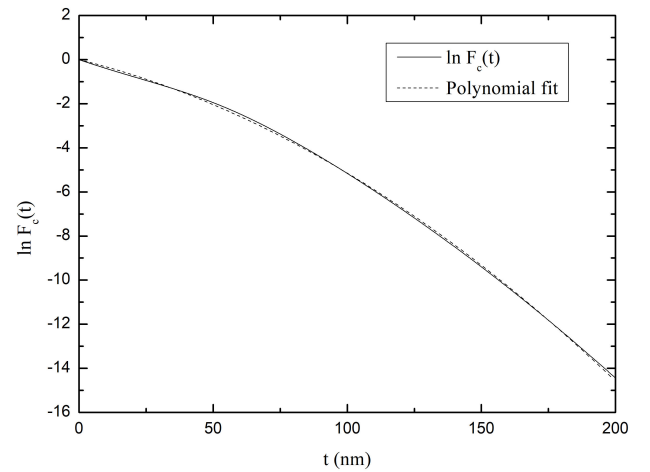


FIGURE 12. Approximation of the “pure” cosine Fourier transform by the function defined by Eq. (27). Note that in the representation it have been used the natural logarithm of  $F_c(t)$  because the corresponding model reduces to an order two polynomial. Solid and dashed lines represent, respectively,  $\ln F_c(t)$  and the best approximating polynomial in the form  $at + bt^2$ .

The use of a particular model to describe the “pure” cosine Fourier transform as a function of the microstructural parameters is more robust but, in the case of the 101 peak of tetragonal zirconia, leads to a meaningless result for  $\langle e^2 \rangle$ . This behaviour is possibly related to the well-known “hook effect” [27, 28], where a concave upward plot of  $F^S(t)$  versus  $t$  is expected and not downward. This effect is traditionally associated to an incorrect estimation of the background or truncation effects. Although, in this example, the peaks are modelled by analytical functions (and, for this reason, the results are less affected by the latter issues), it can not be excluded that the fit of the 101 peak be slightly deficient.

It must be taken into account that area-weighted average column length values obtained by the two procedures are different because the initial-slope method [Eq. (24)] leads to an underestimation of  $\langle t \rangle_a$  [29] with respect to the curve fitting method. In fact, this behaviour is showed in Table IV.

TABLE IV. Microstructural parameters obtained in this study ( $\langle t \rangle_a$  and  $\langle e^2 \rangle$ ). The r.m.s. microstrain was presented instead of its square, according to the traditional rule followed in Crystallography. Symbol - indicates that the value of  $\langle e^2 \rangle$  was negative, providing a result without physical meaning. Numbers between parentheses are the standard deviation referred to the last significant digit. In some cases, uncertainties (derived from error propagation) were unacceptably high -of the order of the value- and it have been omitted. Note that these uncertainties are statistical and don't include possible systematic effects derived from inaccuracies of the models.

Line	Equations (24) and (26)		Equation (27)	
	$\langle t \rangle_a$ (nm)	$\langle e^2 \rangle^{1/2}$	$\langle t \rangle_a$ (nm)	$\langle e^2 \rangle^{1/2}$
101 quartz	24(2)	-	33.29(6)	7.767(6) $10^{-4}$
11-1 m-ZrO <sub>2</sub>	23.3(9)	1.9 $10^{-3}$	32.96(6)	1.6760(2) $10^{-3}$
101 t-ZrO <sub>2</sub>	10.91(9)	-	12.353(7)	-
111 m-ZrO <sub>2</sub>	16.0(5)	1.5 $10^{-3}$	19.25(2)	1.3832(2) $10^{-3}$

Reader must consider that these values are area-weighted and there is a volume-weighted average column length (based in the integral breadth instead of the Fourier analysis), that leads to higher values [4]. Note, moreover, that a correct evaluation of the crystallite size requires a knowledge of the approximate shape of the crystallites.

Although the analysed experimental peaks does not allow to apply a rigorous multiple line method, assuming spherical crystallites with isotropic r.m.s. strain (that is, independent of the crystallographic direction) a double-line procedure [30] could be used with the two peaks of the same phase (11-1 m-ZrO<sub>2</sub> and 111 m-ZrO<sub>2</sub>). However, for the sake of simplicity, this step has been omitted. Note that the application example is not intended for a complete analysis of the microstructure of the selected sample. The main purpose is the application of simple methods of X-ray diffraction microstructural anal-

yses by using the split Voigt function, the main topic in this study.

## 4. Conclusions and summary

Split Voigt functions can be used in X-ray diffraction analyses to determine microstructural features in polycrystalline materials, as other functions traditionally employed (pseudo-Voigt, Pearson VII, Voigt, etc). Due to the extensive use of the Voigt function to describe the shape of the X-ray diffraction lines (justified both theoretically and experimentally), the split Voigt function is a natural extension of the former very useful to modelling asymmetric X-ray diffraction peaks. In this study I have analysed different properties of the split Voigt function (especially interesting in the field of the X-ray diffraction procedures), using that function in the description of the instrumental-spectral peaks to study a sample of quartz and zirconia by single line methods.

## Appendix

### Supplementary material

#### A. Continuity

According to the Eq. (2) the continuity property can be expressed as

$$\frac{I_o \beta_{Cl}}{\exp(k_l^2) \operatorname{erfc}(k_l)} \int_{-\infty}^{+\infty} \frac{\exp\left(-\pi \frac{y^2}{\beta_{Gl}^2}\right)}{\beta_{Cl}^2 + \pi^2 y^2} dy = \frac{I_o \beta_{Cr}}{\exp(k_r^2) \operatorname{erfc}(k_r)} \int_{-\infty}^{+\infty} \frac{\exp\left(-\pi \frac{y^2}{\beta_{Gr}^2}\right)}{\beta_{Cr}^2 + \pi^2 y^2} dy. \quad (\text{A.1})$$

The integrals in the Eq. (A.1) can be easily solved [19], leading to

$$\int_{-\infty}^{+\infty} \frac{\exp\left(-\pi \frac{y^2}{\beta_{Gl}^2}\right)}{\beta_{Cl}^2 + \pi^2 y^2} dy = \frac{\exp(k_l^2) \operatorname{erfc}(k_l)}{\beta_{Cl}}, \quad (\text{A.2})$$

and

$$\int_{-\infty}^{+\infty} \frac{\exp\left(-\pi \frac{y^2}{\beta_{Gr}^2}\right)}{\beta_{Cr}^2 + \pi^2 y^2} dy = \frac{\exp(k_r^2) \operatorname{erfc}(k_r)}{\beta_{Cr}}. \quad (\text{A.3})$$

Substituting Eqs. (A.2) and (A.3) in Eq. (A.1), it can be demonstrated that the maximum of the left half of the split Voigt profile is the same than the maximum of the right half, and equal to  $I_o$  that corresponds to the maximum of the peak. That is, (2) defines a function continuous in all the points.

## B. Integral breadth

According to the Eqs. (2) and (3), we can write

$$\beta = \frac{\beta_{Cl}}{\exp(k_l^2) \operatorname{erfc}(k_l)} \int_{-\infty}^0 \int_{-\infty}^{+\infty} \frac{\exp\left(-\pi \frac{y^2}{\beta_{Gl}^2}\right)}{\beta_{Cl}^2 + \pi^2(x-y)^2} dy dx + \frac{\beta_{Cr}}{\exp(k_r^2) \operatorname{erfc}(k_r)} \int_0^{+\infty} \int_{-\infty}^{+\infty} \frac{\exp\left(-\pi \frac{y^2}{\beta_{Gr}^2}\right)}{\beta_{Cr}^2 + \pi^2(x-y)^2} dy dx. \quad (\text{B.1})$$

Note that each half has an area that is the area of a Voigt function with the same parameters divided by two. In regard to this, the left and right-handed terms in Eq. (B.1) can be substituted by the integral breadths of the corresponding Voigt functions multiplied by 1/2, that is

$$\beta = \frac{\beta_{Gl}}{2 \exp(k_l^2) \operatorname{erfc}(k_l)} + \frac{\beta_{Gr}}{2 \exp(k_r^2) \operatorname{erfc}(k_r)} = \frac{\beta_l + \beta_r}{2}. \quad (\text{B.2})$$

As it could be expected, Eq. (B.2) reduces to the Voigt integral breadth for  $\beta_{Cl} = \beta_{Cr}$  and  $\beta_{Gl} = \beta_{Gr}$ .

## C. Centroid

The centroid of the split Voigt function can be defined as

$$\langle x \rangle = \int_{-\infty}^{+\infty} x sV(x) dx, \quad (\text{C.1})$$

or

$$\langle x \rangle = \int_{-\infty}^0 x sV_l(x) dx + \int_0^{+\infty} x sV_r(x) dx, \quad (\text{C.2})$$

being  $sV_l(x)$  and  $sV_r(x)$ , respectively, the left-handed and right-handed parts of the split Voigt function. The right-handed part is proportional to

$$\int_0^{+\infty} x \int_{-\infty}^{+\infty} \frac{\exp\left(-\pi \frac{(x-y)^2}{\beta_{Gr}^2}\right)}{\beta_{Cr}^2 + \pi^2 y^2} dy dx, \quad (\text{C.3})$$

where the arguments of the Gauss and Cauchy components ( $x - y$  and  $y$ , respectively) have been interchanged with respect to the Eq. (2). Note that this change does not modify the definition of the split Voigt function, due to the properties of the convolution integral.

Integrals in Eq. (C.3) can be interchanged in the following way

$$\int_{-\infty}^{+\infty} \left( \int_0^{+\infty} x \exp\left[-\pi \frac{(x-y)^2}{\beta_{Gr}^2}\right] dx \right) \frac{dy}{\beta_{Cr}^2 + \pi^2 y^2}, \quad (\text{C.4})$$

where

$$\int_0^{+\infty} x \exp\left(-\pi \frac{(x-y)^2}{\beta_{Gr}^2}\right) dx = \frac{1}{2} \left( \frac{\beta_{Gr}^2 \exp\left(-\pi \frac{y^2}{\beta_{Gr}^2}\right)}{\pi} + \beta_{Gr} y + \beta_{Gr} y \operatorname{erf}\left(\frac{\sqrt{\pi} y}{\beta_{Gr}}\right) \right). \quad (\text{C.5})$$

Note that the third term in the right-handed member of the above equation leads to the following integral in  $y$

$$\int_{-\infty}^{+\infty} \frac{\beta_{Gr} y \operatorname{erf}\left(\frac{\sqrt{\pi} y}{\beta_{Gr}}\right) dy}{\beta_{Cr}^2 + \pi^2 y^2}, \quad (\text{C.6})$$

that does not converge in the  $[-\infty, +\infty]$  interval. A similar result is obtained by examining the left-handed part of the Eq. (C.2). This means that the centroid of the split Voigt function is not well defined. As consequence, the variance about the centroid is also not well defined, as in the case of the Cauchy function [19].

## D. Fourier transform

Equation (21), according to the expression (2), translates to

$$F(t) = \frac{I_o\beta_{Cl}}{\exp(k_l^2) \operatorname{erfc}(k_l)} \int_{-\infty}^0 \int_{-\infty}^{+\infty} \frac{\exp\left(-\pi \frac{y^2}{\beta_{Cl}^2}\right)}{\beta_{Cl}^2 + \pi^2(x-y)^2} \exp(2\pi ixt) dy dx$$

$$+ \frac{I_o\beta_{Cr}}{\exp(k_r^2) \operatorname{erfc}(k_r)} \int_0^{+\infty} \int_{-\infty}^{+\infty} \frac{\exp\left(-\pi \frac{y^2}{\beta_{Cr}^2}\right)}{\beta_{Cr}^2 + \pi^2(x-y)^2} \exp(2\pi ixt) dy dx, \quad (\text{D.1})$$

or

$$F(t) = \frac{I_o\beta_{Cl}}{\exp(k_l^2) \operatorname{erfc}(k_l)} \int_{-\infty}^0 \int_{-\infty}^{+\infty} \frac{\exp\left(-\pi \frac{(x-y)^2}{\beta_{Cl}^2}\right)}{\beta_{Cl}^2 + \pi^2 y^2} \exp(2\pi ixt) dy dx$$

$$+ \frac{I_o\beta_{Cr}}{\exp(k_r^2) \operatorname{erfc}(k_r)} \int_0^{+\infty} \int_{-\infty}^{+\infty} \frac{\exp\left(-\pi \frac{(x-y)^2}{\beta_{Cr}^2}\right)}{\beta_{Cr}^2 + \pi^2 y^2} \exp(2\pi ixt) dy dx. \quad (\text{D.2})$$

In Eq. (D.2) we can examine first the left-handed term. In this way, interchanging the integrals, we have

$$\frac{I_o\beta_{Cl}}{\exp(k_l^2) \operatorname{erfc}(k_l)} \int_{-\infty}^0 \int_{-\infty}^{+\infty} \frac{\exp\left(-\pi \frac{(x-y)^2}{\beta_{Cl}^2}\right)}{\beta_{Cl}^2 + \pi^2 y^2} \exp(2\pi ixt) dy dx$$

$$= \frac{I_o\beta_{Cl}}{\exp(k_l^2) \operatorname{erfc}(k_l)} \int_{-\infty}^{+\infty} \int_{-\infty}^0 \exp\left(-\pi \frac{(x-y)^2}{\beta_{Cl}^2}\right) \exp(2\pi ixt) dx [\beta_{Cl}^2 + \pi^2 y^2]^{-1} dy. \quad (\text{D.3})$$

The integral in  $x$  in Eq. (D.3) can be developed as

$$\int_{-\infty}^0 \exp\left(-\pi \frac{(x-y)^2}{\beta_{Cl}^2}\right) \exp(2\pi ixt) dx = \frac{\beta_{Cl}}{2} \exp(-\pi\beta_{Cl}^2 t^2) \exp(2\pi iyt) \left(1 - i \operatorname{erfi}\left[\sqrt{\pi}\beta_{Cl}t - \frac{\sqrt{\pi}}{\beta_{Cl}}iy\right]\right), \quad (\text{D.4})$$

$\operatorname{erfi}(z)$  being the imaginary error function

$$\operatorname{erfi}(z) = \frac{\operatorname{erf}(iz)}{i}. \quad (\text{D.5})$$

Thus, Eq. (D.3) can be expressed as

$$\frac{I_o\beta_{Cl}}{\exp(k_l^2) \operatorname{erfc}(k_l)} \frac{\beta_{Cl}}{2} \exp(-\pi\beta_{Cl}^2 t^2) \int_{-\infty}^{+\infty} \frac{\exp(2\pi iyt)}{\beta_{Cl}^2 + \pi^2 y^2} \left(1 - \operatorname{erf}\left[\frac{\sqrt{\pi}}{\beta_{Cl}}y + \sqrt{\pi}\beta_{Cl}ti\right]\right) dy, \quad (\text{D.6})$$

that it can be written as

$$\frac{I_o\beta_{Cl}}{\exp(k_l^2) \operatorname{erfc}(k_l)} \frac{\beta_{Cl}}{2} \exp(-\pi\beta_{Cl}^2 t^2) \left(\int_{-\infty}^{+\infty} \frac{\cos(2\pi yt)}{\beta_{Cl}^2 + \pi^2 y^2} dy - \int_{-\infty}^{+\infty} \frac{\exp(2\pi iyt)}{\beta_{Cl}^2 + \pi^2 y^2} \operatorname{erf}\left[\frac{\sqrt{\pi}}{\beta_{Cl}}y + \sqrt{\pi}\beta_{Cl}ti\right] dy\right). \quad (\text{D.7})$$

taking into account that the integral

$$\int_{-\infty}^{+\infty} \frac{\sin(2\pi yt)}{\beta_{Cl}^2 + \pi^2 y^2} dy, \quad (\text{D.8})$$

vanish due to the odd character of the sine function. In regard to this, after some manipulation, Eq. (D.3) can be expressed as

$$\frac{I_o\beta_{Cl}}{\exp(k_l^2) \operatorname{erfc}(k_l)} \frac{\beta_{Cl}}{2} \exp(-\pi\beta_{Cl}^2 t^2) \left(\beta_{Cl}^{-1} \exp(-2\beta_{Cl}t) - \int_{-\infty}^{+\infty} \frac{\exp(2\pi iyt)}{\beta_{Cl}^2 + \pi^2 y^2} \operatorname{erf}\left[\frac{\sqrt{\pi}}{\beta_{Cl}}y + \sqrt{\pi}\beta_{Cl}ti\right] dy\right). \quad (\text{D.9})$$

It can be proved that the integral containing the error function provides the imaginary part of Eq. (D.3), although it can not be expressed in a simple form, as in the case of the real part. In a similar way, the right-handed term of Eq. (D.2) can be written as

$$\frac{I_o\beta_{Cr}}{\exp(k_r^2) \operatorname{erfc}(k_r)} \frac{\beta_{Cr}}{2} \exp(-\pi\beta_{Cr}^2 t^2) \left(\beta_{Cr}^{-1} \exp(-2\beta_{Cr}t) + \int_{-\infty}^{+\infty} \frac{\exp(2\pi iyt)}{\beta_{Cr}^2 + \pi^2 y^2} \operatorname{erf}\left[\frac{\sqrt{\pi}}{\beta_{Cr}}y + \sqrt{\pi}\beta_{Cr}ti\right] dy\right), \quad (\text{D.10})$$

also being the integral containing the error function the corresponding imaginary part of the Eq. (D.10). Now, the sum of the left- and right-handed parts is

$$FT(t) = \frac{I_o\beta_{Cl}}{\exp(k_l^2)\operatorname{erfc}(k_l)} \frac{\beta_{Gl}}{2} \exp(-\pi\beta_{Gl}^2t^2) \left( \beta_{Cl}^{-1} \exp(-2\beta_{Cl}t) - \int_{-\infty}^{+\infty} \frac{\exp(2\pi iyt)}{\beta_{Cl}^2 + \pi^2y^2} \operatorname{erf} \left[ \frac{\sqrt{\pi}}{\beta_{Gl}}y + \sqrt{\pi}\beta_{Gl}ti \right] dy \right) \\ + \frac{I_o\beta_{Cr}}{\exp(k_r^2)\operatorname{erfc}(k_r)} \frac{\beta_{Gr}}{2} \exp(-\pi\beta_{Gr}^2t^2) \left( \beta_{Cr}^{-1} \exp(-2\beta_{Cr}t) + \int_{-\infty}^{+\infty} \frac{\exp(2\pi iyt)}{\beta_{Cr}^2 + \pi^2y^2} \operatorname{erf} \left[ \frac{\sqrt{\pi}}{\beta_{Gr}}y + \sqrt{\pi}\beta_{Gr}ti \right] dy \right). \quad (\text{D.11})$$

Note, as I have pointed out, that the imaginary part can not be expressed in terms of simple analytical functions.

## Acknowledgements

Thanks are due to the Junta de Extremadura and the European Regional Development Fund by its support under the project GR21012.

- 
- i. <https://www.bruker.com/en/products-and-solutions/diffractometers-and-x-ray-microscopes/x-ray-diffractometers/diffrac-suite-software/diffrac-topas.html>
  - ii. <https://fityk.nieto.pl/model.html>
  - iii. The experimental profile,  $h(x)$ , is defined, in the framework of the kinematical diffraction theory, as the convolution product of the instrumental-spectral profile,  $g(x)$ , and the “pure” microstructural profile,  $f(x)$ , by means of  $h(x) = \int g(x - y)f(y)dy$ .
  - iv. It is assumed that the Fourier transform is normalized as indicated in Subsection 2.6
1. H. C. van de Hulst and J. J. M. Reesinck, Line breadths and Voigt profiles, *ApJ* **106** (1947) 121,
  2. P. Suortti, M. Ahtee and L. Unonius, Voigt Function Fit of X-ray and Neutron Powder Diffraction Profiles, *J. Appl. Cryst.* **12** (1979) 365,
  3. Th. H. de Keijser, J. I. Langford, E. J. Mittemeijer and A. B. P. Vogels, Use of the Voigt Function in a Single-Line Method for the Analysis of X-ray Diffraction Line Broadening, *J. Appl. Cryst.* **15** (1982) 308,
  4. D. Balzar and H. Ledbetter, Voigt-Function Modeling in Fourier Analysis of Size- and Strain-Broadened X-ray Diffraction Peaks, *J. Appl. Cryst.* **26** (1993) 97,
  5. J. I. Langford, A Rapid Method for Analysing the Breadths of Diffraction and Spectral Lines using the Voigt Function, *J. Appl. Cryst.* **11** (1978) 10,
  6. P. Thompson, D. E. Cox and J. B. Hastings, Rietveld Refinement of Debye-Scherrer Synchrotron X-ray Data from  $\text{Al}_2\text{O}_3$ , *J. Appl. Cryst.* **20** (1987) 79,
  7. M. M. Hall, V. G. Veeraraghavan, H. Rubin and P. G. Winchell, The approximation of symmetric X-ray peaks by Pearson type VII distributions, *J. Appl. Cryst.* **10** (1977) 66,
  8. J. Rodríguez-Carvajal, Recent advances in magnetic structure determination by neutron powder diffraction, *Physica B* **192** (1993) 55,
  9. B. H. Toby and R.B. Von Dreele, GSAS-II: the genesis of a modern open-source all purpose crystallography software package, *J. Appl. Cryst.* **46** (2013) 544,
  10. R. A. Young *et al.*, The Rietveld Method (International Union of Crystallography, Oxford University Press, Oxford, 1993).
  11. L. Lutterotti, Total Pattern Fitting for the Combined Size-Strain-Stress-Texture Determination in Thin Film Diffraction, *Nucl. Instrum. Methods Phys. Res. B* **268** (2010) 334,
  12. Y. H. Dong and P. Scardi, MarqX: a new program for whole-powder-pattern fitting, *J. Appl. Cryst.* **33** (2000) 184,
  13. R. W. Cheary and A. A. Coelho, Axial Divergence in a Conventional X-ray Powder Diffractometer. I. Theoretical Foundations, *J. Appl. Cryst.* **31** (1998) 851,
  14. E. Michalski, The Diffraction of X-rays by Close-Packed Polytropic Crystals Containing Single Stacking Faults. I. General Theory, *Acta Cryst. A* **44** (1988) 640,
  15. H. Flores-Llamas, Asymmetries of the Voigt line shape, *J. Appl. Cryst.* **34** (2001) 136,
  16. M. J. Wojdyr, Fityk: A general-purpose peak fitting program, *J. Appl. Cryst.* **43** (2010) 1126,
  17. N. C. Halder and C. N. J. Wagner, Separation of particle size and lattice strain in integral breadth measurements, *Acta Cryst.* **20** (1966) 312,
  18. W. H. Press, S. A. Teukolsky, W. T. Vetterling and B. P. Flannery, Numerical Recipes in Fortran 77: The Art of Scientific Computing (Cambridge University Press, New York, 1992).
  19. M. Abramowitz, and I. A. Stegun, Handbook of Mathematical Functions (Dover publications Inc., New York, 1972).
  20. D. W. Posener, The shape of spectral lines: tables of the Voigt profile  $\frac{a}{\pi} \int_{-\infty}^{+\infty} [\exp(-y^2)dy/a^2 + (v - y)^2]$ , *Aust. J. Phys.* **12** (1959) 184,
  21. J. Pantoja-Cortés, F. Sánchez-Bajo and A. L. Ortiz, Evaluating nanocrystalline size distributions in doped and undoped nanocrystalline ceramics by X-ray diffractometry, *Ceram. Int.* **44** (2018) 22365,
  22. P. Scardi and M. Leoni, Whole powder pattern modelling, *Acta Cryst. A* **A58** (2002) 190,

23. G. K. Williamson and W. H. Hall, X-ray line broadening from filed aluminium and wolfram, *Acta Metall.* **1** (1953) 22,
24. B. E. Warren and B. L. Averbach, The Effect of Cold-Work Distortion on X-Ray Patterns, *J. Appl. Phys.* **21** (1950) 595,
25. Th. H. de Keijser, E. J. Mittemeijer and H. C. F. Rozendaal, The Determination of Crystallite-Size and Lattice-Strain Parameters in Conjunction with the Profile-Refinement Method for the Determination of Crystal Structures, *J. Appl. Cryst.* **16** (1983) 309,
26. R. Delhez, Th. H. de Keijser and E. J. Mittemeijer, Determination of Crystallite Size and Lattice Distortions through X-ray Diffraction Line Profile Analysis, *Fresenius Z. Anal. Chem.* **312** (1982) 1,
27. H. P. Klug and L. E. Alexander, X Ray Diffraction Procedures for Polycrystalline and Amorphous Materials (Wiley-Interscience Publication, 1974).
28. P. Dasgupta, On the intrinsic hook effect associated with pseudo-Voigt profiles, *J. Appl. Cryst.* **35** (2002) 267,
29. R. K. Nandi, H. K. Kuo, W. Schlosberg, G. Wissler, J. B. Cohen and B. Crist Jr, Single-Peak Methods for Fourier Analysis of Peak Shapes, *J. Appl. Cryst.* **17** (1984) 22,
30. A. L. Ortiz, F. Sánchez-Bajo, A. Hernández-Jiménez, F. Guiberteau and F.L. Cumbreira, X-ray line-broadening study of a liquid-phase-sintered silicon carbide, *J. Eur. Ceram. Soc.* **22** (2002) 2677,